Supplemental Information for:

Waves of maturation and senescence in micro-structural MRI markers of human cortical myelination over the lifespan

Håkon Grydeland[a], Petra E. Vértes[b], František Váša[b], Rafael Romero-Garcia[b], Kirstie Whitaker[b,c], Aaron F. Alexander-Bloch[b], Atle Bjørnerud[a,d], Ameera X. Patel[b], Donatas Sederevicius[a], Christian K. Tamnes[e], Lars T. Westlye[e], Simon Rx. White[f], Kristine B. Walhovd[a,d], Anders M. Fjell[a,d,1], Edward T. Bullmore[b,g,h,i, 1]

[a] Research Group for Lifespan Changes in Brain and Cognition, Department of Psychology, University of Oslo, 0317 OSLO, Norway
[b] Department of Psychiatry, University of Cambridge, Cambridge, CB2 0SZ, UK
[c] The Alan Turing Institute, London, NW1 2DB, UK
[d] Department of Physics, University of Oslo, 0371 OSLO, Norway
[e] Department of Psychology, University of Oslo, 0317 OSLO, Norway
[f] MRC Biostatistics Unit, University of Cambridge, Cambridge CB2 0SR, UK
[g] Cambridgeshire and Peterborough NHS Foundation Trust, Huntingdon, PE29 3RJ, UK
[h] MRC/Wellcome Trust Behavioural and Clinical Neuroscience Institute, University of Cambridge, Cambridge, CB2 3EB, UK
[i] Immuno-Inflammation Therapeutic Area Unit, GlaxoSmithKline R&D, Stevenage SG1 2NY, UK

[1] A.M.F and E.T.B contributed equally to this work.

Corresponding author: Håkon Grydeland, Department of Psychology, University of Oslo, PO Box 1094 Blindern, 0317 OSLO, Norway, phone: +4722845093, email: hakon.grydeland@psykologi.uio.no

Contents

Supplementary Methods

Sample. The Regional Committee for Medical and Health Research Ethics of South Norway approved the study. We drew the sample mainly from the first wave of 2 on-going longitudinal projects by the Research Group for Lifespan Changes in Brain and Cognition at the University of Oslo, namely *Neurocognitive Development*, and *Cognition and Plasticity through the Lifespan*. Participants were recruited through newspaper ads, among students and employees at the University of Oslo, and from local schools. Further details regarding recruitment and enrolment can be found elsewhere (1-3). Participants under 12 years of age gave oral informed consent, while written informed consent was obtained from all participants from 12 years of

age and from a parent or guardian for participants below 18 years of age. Parents of children younger than 16 years, and all participants aged 16 years or older, were screened with standardized health interviews at enrolment to ascertain eligibility. We required participants to be right-handed, fluent Norwegian speakers, and have normal or corrected to normal vision and hearing. Self-reported neurological or psychiatric conditions known to affect normal cerebral functioning, including clinically significant stroke, traumatic brain injury, untreated hypertension, diabetes, use of psychoactive drugs within the last 2 years, or subjective concerns about cognitive status including memory function, were used as exclusion criteria. All participants above 20 years of age scored < 16 on the Beck Depression Inventory (4) and participants above 40 years of age scored ≥ 26 on Mini Mental State Examination (5). A neuroradiologist evaluated and deemed all scans free of significant injuries or conditions. Based on the existence of a T1-weighted and a T2-weighted scan for each individual, and after quality control excluding a total of 18 participants due to overfolding movement articfacts in T1w, T2w, or both, or missing/incomplete T2w scan, we included 484 participants: 263 females (54.3%), mean age (SD) = 38.3 (22.5) years, median age= 34.6 years, age range = 8.2-85.4 years. Of these, 73 new participants were included relative to our previous work (6): 37 females (50.7%), mean age = 15.4, SD = 3.3, median age= 15.4, min-max age = 9.1-21.6. All participants underwent assessment of general cognitive abilities by the Wechsler Abbreviated Scale of Intelligence (WASI) (7). Estimated mean full-scale intelligence quotient for the entire sample was 112.9 (SD = 9.9, range = 82–145).

MRI Data Acquisition. All scans were acquired using a 12-channel head coil on a 1.5-T Siemens Avanto scanner (Siemens Medical Solutions, Erlangen, Germany) at Oslo University Hospital Rikshospitalet. For each participant, the T1w and the T2w scans was acquired in the same session. The T1w volumes were acquired using a 3D T1w magnetization-prepared rapid gradient echo (MPRAGE) sequence with the following parameters; repetition time (TR) = 2400 ms, echo time (TE) = 3.61 ms, inversion time (TI) = 1000 ms, 8° flip angle (FA), bandwidth = 180 Hz/pixel, field of view (FOV) = 240 mm, matrix = 192 × 192 × 160, 1.25 × 1.25 × 1.2 mm voxels. The T2w volumes were acquired using a 3D T2w sampling perfection with application optimized contrasts using different flip angle evolutions (SPACE) sequence with the

following parameters: TR = 3390 ms, TE = 388 ms, variable FA, bandwidth = 650 Hz/pixel, FOV = 256 mm, 1 mm isotropic voxels. One hundred seventy-four participants (53.4% female) were scanned with a 204 × 256 × 176 matrix (mean age (SD) = 35.2 (19.5), range = 8.2-60.6), while 310 participants (54.8% female) were scanned with a 256 × 256 × 176 matrix (mean age (SD) = 40.0 (23.9), range = 8.5-85.4). Both T1w and T2w scans were acquired sagittally.

Creation of T1w/T2w Maps. T1w/T2w ratio maps for each participant were created by running the T1w and T2w images through the Human Connectome Project (HCP) processing pipeline (8), using scripts kindly made available online by HCP (https://github.com/Washington-University/Pipelines). Via the HCP pipeline, the T1w volumes were processed using the Freesurfer 5.3 suite (http://surfer.nmr.mgh.harvard.edu), including intensity normalization, automated tissue segmentation, generation of white and pial surfaces, surface topology correction, and surface-based cortical thickness and mean curvature maps (10-16). In the preprocessing step, we did not perform the gradient distortion correction as scanning was performed on a conventional scanner (Siemens Avanto) compared with the custom scanner used in the HCP (8) (we tested this additional step for one participant, the output looked very similar). Data was gathered without field map, so no readout distortion correction was performed. As noted in Glasser*, et al.* (8), this step removes a fairly subtle readout distortion, most pronounced in regions with high B0 inhomogeneity due to magnetic susceptibility differences (orbitofrontal cortex and inferior temporal cortex especially) (9). However, interpretation of effects, or lack thereof, in these areas should be made with caution.

The T2w image was registered to the T1w image by using Freesurfer's *bbregister*, a within-subject, cross-modal registration using a boundary-based cost function constrained to be 6 degrees of freedom (rigid body) (17). As in our previous work, but here via the HCP pipeline, the resulting linear transform was applied by use of FSL's *applywarp* tool using spline interpolation in order to minimize the white matter and cerebrospinal fluid (CSF) contamination of GM voxels (18). The T1w volume was divided on the aligned T2w volume, creating a T1w/T2w ratio volume.

To estimate regional T1w/T2w ratio across the brain, we used a multi-modal parcellation of the cortex into 180 symmetrical areas per hemisphere (19). The parcellation was mapped into each participant's native space to minimize geometric deformation of the data by inverting the warp from each participant to a common surface using a non-rigid high-dimensional spherical averaging method to align cortical folding patterns (20). Multimodal Surface Matching (21) was not performed as i) participants between 40 and 60 did not having a resting-state functional MRI scan, and ii) as the T1w/T2w maps were being used as a measure of interest, we did not want to include these data in the registration process, and thereby potentially influence the registration based on differences in T1w/T2w values.

Intracortical Depth. From the resulting 360 cortical surface regions, the T1w/T2w ratio was extracted using the *wb_command -volume-to-surface-mapping* using cubic splines interpolation. We sampled T1w/T2w values vertex-wise from the WM/GM boundary, from 9 intracortical depths at 10% intervals, and at the grey matter (GM)/CSF boundary (pial), resulting in 11 surfaces. Each surface was obtained by using the *-surface-cortex-layer* command, which takes effects of folding into account, and thus follows the cortical layers more closely. **Fig. S8** shows higher T1w/T2w values at lower depths. As the surfaces near the WM/GM boundary and the GM/CSF boundary, respectively, suffer more from partial voluming effects (22), that is voxels being composed of different tissue types, we focused on the 30-70% depths (22, 23). From these middle depths, we chose the depth in which the age-relationships showed the lowest residual sums of squares (across regions), which was the 70% depth from the WM/GM boundary (**Fig. S9)**. Although we cannot precisely determine cortical layers, and at this resolution we obtain information from more than one layer, the 70% depth corresponds (on average) to layer 3 (24). Layer 3 has intracortical projections, that is, horizontal corticocortical projections traveling within the grey matter of the cerebral cortex based on work in the dorsolateral prefrontal cortex (25). Although all pyramidal neurons have connections within the cerebral cortex, the prominent source of distant intracortical projections arise mainly from pyramidal neurons within layers 2 and 3, and a sub-set of neurons in layers 5 and 6 (24). Further, layer 2 and superficial layer 3 have been shown to contain intrinsic pyramidal neuron projections (in prefrontal areas 9 and 46) which make long distance lateral

connections to patches of tissue in layers 1-3. Laterally travelling fibers are primarily in layers 2 and superficial 3, with oblique descending collaterals through layer 3. Pyramidal neurons of layer 3 also give rise to prominent horizontal projections with periodic terminations in layers 1-3 (see for instance figure 17 in (26)).

In each of the 360 regions, outliers within each region for a single participant, and across participants, were identified as values exceeding the following formula using first (Q1), and third (Q3) quantiles, and the interquartile range (IQR): Q1-IQR*1.5, and Q3+IQR*1.5. These values were excluded.

Correction for T2w differences. To take into account the minor difference in acquisition parameters for the T2w scans (174 participants were scanned with a 204 $\times$ 256 $\times$ 176 matrix, while 310 participants were scanned with a 256 $\times$ 256 $\times$ 176 matrix), we estimated the effect of matrix in the developmental part of the sample where participants of overlapping ages were scanned with either one of the matrices (n_{204} = 67 (47.7% females), mean age (SD) = 13.4 (2.9), min-max = 8.2-18 versus n_{256} = 72 (50% females), mean age (SD) = 13.7 (2.6), min-max = 8.5-18). The effect was estimated running a robust regression using the Andrews weight function and the default tuning constant of 1.339 as implemented in Matlab, yielding coefficient estimates that are approximately 95% as statistically efficient as the ordinary least-squares estimates (provided the response has a normal distribution with no outliers). Age, sex, and an interaction term of age $\times$ matrix dimension were included as covariates of no interest. The estimated effect was then added to the 174 participants scanned with the 204 $\times$ 256 $\times$ 176 matrix.

Estimations of Growth Curve Trajectories. To fit age trajectories without assuming a specific shape, for instance, linear, or quadratic, of the lifespan relationship *a priori*, we chose to use penalized cubic B-splines (27, 28). Eight piecewise cubic B-spline basis functions were used, which was the lowest possible value in which all 360 models produced a fit. **Fig. S10** shows a penalized cubic B-spline growth curve fitted to simulated data, and the 8 underlying basis functions, multiplied by their respective coefficients. The fitted growth curve stem from a weighted sum of these basis functions (see also Alexander-Bloch*, et al.* (29)). The knots were placed at quantiles

of the distribution of unique age values. The value for the smoothing parameter yielding appropriate degree of smoothness was found using restricted maximum likelihood (REML) (30). REML was chosen as REML appear less prone to local minima than the generalized cross validation (30), which resulted in a smoother derivative, and thus milestone estimates less affected by minor variations. Note that this choice effectively imposes prior beliefs about the correct model. For instance, in the extreme case, a model passing through all data points would *a priori* be considered as not biologically plausible as it would not transition smoothly across the age range. Thus, although the model structure allows considerable flexibility, we chose to penalize excessively fluctuating models, i.e. that are not biologically plausible (27). The median effective degrees of freedom was 5.7 (range = 3.5-6.9).

The derivative of the fitted penalized cubic B-spline growth curve was obtained by calculating the slope at each point along the curve using the *diff* function in R. Specifically, the derivative was taken as the differences (Δy) between the predicted growth curve (using the *predict* function) from i) one set of age values, and ii) a set of slightly increased (0.08 years) age values, divided by this 0.08 increment in age (Δx): $\frac{\Delta y}{\Delta x}$ or $\frac{dy}{dx}$. This calculation yielded a point estimate at each point along the growth curve. We wanted to know at which ages the increases or decreases were sufficient to be considered statistically significant. Therefore, we estimated 99.99% confidence interval of the derivative. This level was used in order to yield conservative estimates, as the confidence interval is correct at each point, but liberal if looking at several points (that is, not corrected for familywise error). These confidence intervals were obtained as implemented in *predict.gam* (31) in R (https://cran.r-project.org), using the Bayesian posterior covariance matrix, and multiplying the derivatives (in matrix form, for each smooth term) with this covariance matrix, before multiplying this product with the derivatives. To obtain the standard error for the entire spline, and not for each of the basis functions that comprise the spline, the resulting values were summed across spline terms, and their square root taken.

Based on the confidence interval of the derivative, we extracted 3 curve features, or milestones, namely age at peak growth, age at onset of stability, and age at onset of decline. Peak growth age was defined as the maximum positive value. Onset of

stability age was the first point showing a non-significant slope, that is, the age at which the lower confidence interval crossed zero for the first time. Onset of decline age was the point where the curve again showed a significant slope, that is, the age at which the upper confidence interval crossed zero. We also estimated cross-sectional measures of the rate of growth, and the rate of decline (**Fig. S1**). For the rate of growth, we extracted the derivative at peak growth age. The rate of decline was also extracted from the derivative, at age A in the following manner: the sum of i) onset decline age, for instance 60 years, and ii) the age at the halfway point (50%) between a) onset decline age, and b) maximum age in the sample, for instance: (85-60) $\times$ 0.5 = 12.5, which in this example would yield A = 60 + 12.5 = 72.5 years as the age of measurement. As the derivative is the slope between 2 points, all values were taken as the average between the value and the successive value. The procedure of estimating the spline, calculating the derivative and confidence intervals, and obtaining milestones was repeated for each of 360 regions.

Test of unimodality. For each of the milestone distributions, we tested forunimodality using Hartigans' dip test statistic for unimodality (32) in R using the *diptest* package. As the dip test yields very conservative p-values (33), we simulated P values from the unimodal distribution closest to the data (34) using the *fpc* package. An indication of non-unimodality, that is, at least bimodal distributions was deemed present if the tests were significant ($P < 0.05$). To further validate this result, we used an expectation–maximization (EM) algorithm to fit Gaussian finite mixture models with 1 and 2 components (a maximum of 2 components would provide proof of concept, and not be liable to over-fitting) as implemented in the R package *mclust*, and tested for best fit using a bootstrap likelihood ratio test with 10000 bootstraps. We fitted an EM algorithm (**Fig. 2B**), as employed in the R package *mixtools* which yielded parameters for mu and sigma, for visualization. The fit was qualitatively deemed good (except for the second mode in M3, which, however, clearly stood out), and we proceeded with exploratory analyses dichotomizing the 3 milestones. The age used to separate the two waves in each distribution was obtained by visual inspection of the point where the density functions crossed (the second mode in M3 was identified as the late wave).

To describe the cognitive functions of regions showing the different wave properties we used NeuroSynth (http://neurosynth.org), a data-driven tool that mines the published neuroimaging literature and provides terms most likely to be used in publications alongside specific MRI coordinates (35). For this study we passed the two wave maps (early and late) for each milestone to the NeuroSynth decoder and visualised the top 25 terms related to the highlighted regions as a word cloud. The size and colour saturation of the words in **Fig. 2D** correspond to the frequencies associated with each term.

Comparison with the histological cytoarchitectural map of von Economo and Koskinas. Following van den Heuvel, Scholtens, Feldman Barrett, Hilgetag and de Reus (36) and Vertes, et al. (37), we explored the relationship between cortical histology and the three key milestones. To this end, based on Scholtens, de Reus, de Lange, Schmidt and van den Heuvel (38) and Solari and Stoner (24), we assigned each of the 360 regions to 1 of 5 cytoarchitectonic types classified according to the scheme of von Economo and Koskinas (39), reflecting the 5 structural types of isocortex, namely homotypic, or type 2, 3 and 4, and heterotypic, or type 1 agranular and type 5 granular. Again following Vertes, et al. (37), as the original classification of structural types does not discriminate between true six-layered isocortex, and mesocortex or allocortex, we defined two additional subtypes: limbic cortex which included the entorhinal, retrosplenial, presubicular and cingulate cortices, and thus primarily constitutes allocortex, and the insular cortex which contains granular, agranular and dysgranular regions, and is therefore not readily assigned a single structural type. Structural classes were manually assigned to each region in Scholtens et al.'s parcellation, based on Figure 3 in Solari and Stoner (24), Figure 1F in Vertes, et al. (37), and anatomical landmarks. Each of the 360 used here was then assigned a class based on overlap with the Scholtens et al. parcellation. In cases of overlap with more than one class, the region was assigned the class with which it overlapped the most.

Structural Network Analyses. To investigate how the milestones, which are local in nature, might relate to global network properties of the brain, we employed a structural covariance approach (40). We correlated T1w/T2w for each region with all

other regions, across participants between the ages of maturity and decline onset in the global curve (see **Fig. 1B**; 37 and 69 years, respectively), that is, a period with relative stable T1w/T2w levels. This procedure yielded a 360×360 connectivity matrix, which was binarized employing a minimum spanning tree approach followed by global thresholding, retaining 10% of the strongest connections or edges (**Fig. S6A**) (41). From this model, we assessed two of the most common network metrics, namely degree and modularity. These analyses were carried out in Matlab (https://www.mathworks.com) using the Brain Connectivity Toolbox (42). Degree refers to the number of edges for each region (node). The degree distribution was fat-tailed (**Fig. S6C**), indicating the presence of high-degree regions, so-called hubs. Modularity measures community structure, or to what extent nodes aggregate into smaller groups hallmarked by being more interconnected between members of the groups than across groups. Here, modularity was calculated using the Louvain algorithm (43), using consensus clustering (44). The choice of resolution parameter for modular decomposition, γ, which usually is set to 1, was empirically defined by finding a local minimum for nodal versatility of modular affiliation (45), to identify values of γ at which nodes are consistently assigned to the same module. After calculating versatility from γ = 0.1 to 4, with 0.01 increments, we chose the gamma which minimized versatility, here γ = 1.12. Based on the final community partition (**Fig. S6B)**, we also evaluated the intra- and intermodule degree, that is connections within a node's community, and across other communities, respectively. A network representation of the structural connectivity (**Fig. 4ii)** was visualised using NetworkX, version 2.1 (https://networkx.github.io).

Statistical Analyses. Relationships between various node measures (for instance average T1w/T2w, and milestones) were tested using Spearman's rank correlation, except between rate of maturation and decline, where a linear regression was performed. To test for differences in rates of growth and decline, respectively, between early and late waves across the 3 milestones, we calculated 95% confidence intervals. In the cases where the confidence interval overlapped, we tested for differences between waves by Wilcoxon rank sum test. The same approach was used to test for differences in the degree measures between waves. To test for the differences across cytoarchitectonic classes, we employed Kruskal-

Wallis tests by rank, a non-parametric alternative to an analysis of variance (ANOVA). Here, to account for the multiple tests performed, false discovery rate (FDR) correction was applied using the method of Benjamini, and Yekutieli (46) via the p.adjust function in R.

Supplementary Tables

Supplementary Table 1

		Rate (x 10^{-2})		Degree		
		Maturation	Decline	Total	Intramodular	Intermodular
M1	Wave1	1.56 [1.44,1.69]	-1.04 [-1.21,-0.90]	11 [8,17]	6 [5,9]	5 [3,9]
	Wave2	1.14 [1.09,1.19]	-0.76 [-0.84,-0.68]	41 [37,45]	21 [19,23]	19 [17,22]
M2	Wave1	1.31 [1.26,1-36]	-0.93 [-1.01,-0.85]	35 [31,40]	19 [17,21]	16 [14,19]
	Wave2	0.86 [0.79,0.93]	-0.40 [-0.48,-0.32]	39 [31,47]	20 [16,24]	19 [14,24]
M3	Wave1	1.45 [1.39,1.52]	-1.25 [-1.34,-1.16]	31 [26,36]	17 [15,20]	14 [11,18]
	Wave2	0.99 [0.94,1.04]	-0.40 [-0.47,-0.34]	41 [35,46][w]	21 [18,24][x]	20 [17,23][y]

95% confidence intervals were calculated using the adjusted bootstrap percentile method (10000 bootstraps replicates) using the R package *rcompanion*.

[w] Wilcoxon rank sum test between wave 1 and 2: W = 13427, P = 0.006 (two-sided).

[x] W = 14224, P = 0.050.

[y] W = 13496, P = 0.006.

Supplementary Figures

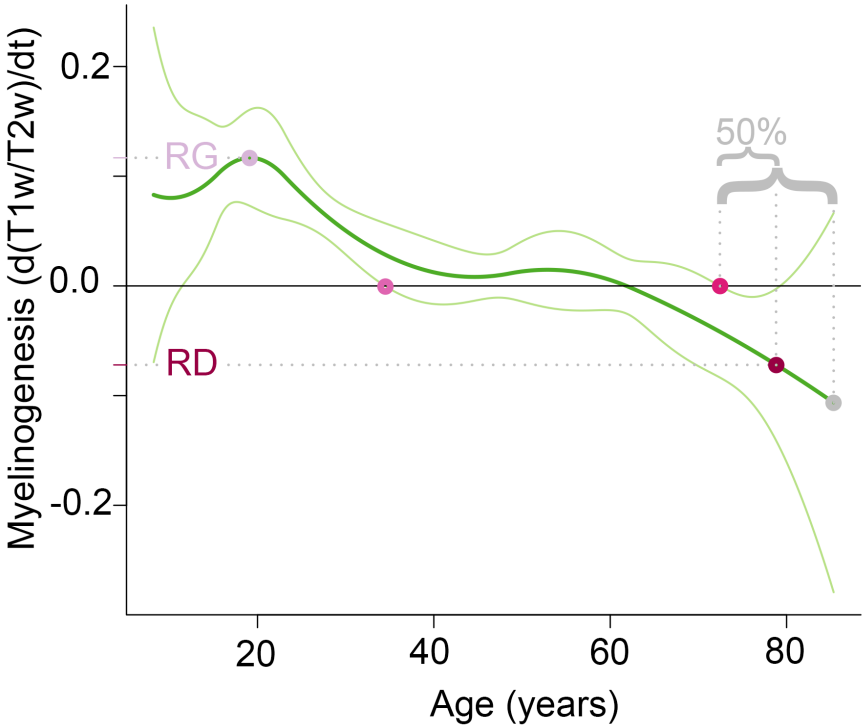

Fig. S1. Derivative of average curve in **Fig. 1B** (main text), showing rate of growth (RG), and rate of decline (RD) points. The rate of growth was obtained from the point of peak growth, and RD was obtained at the halfway-point (50% of the distance) between the onset of decline age and the maximum age in the sample.

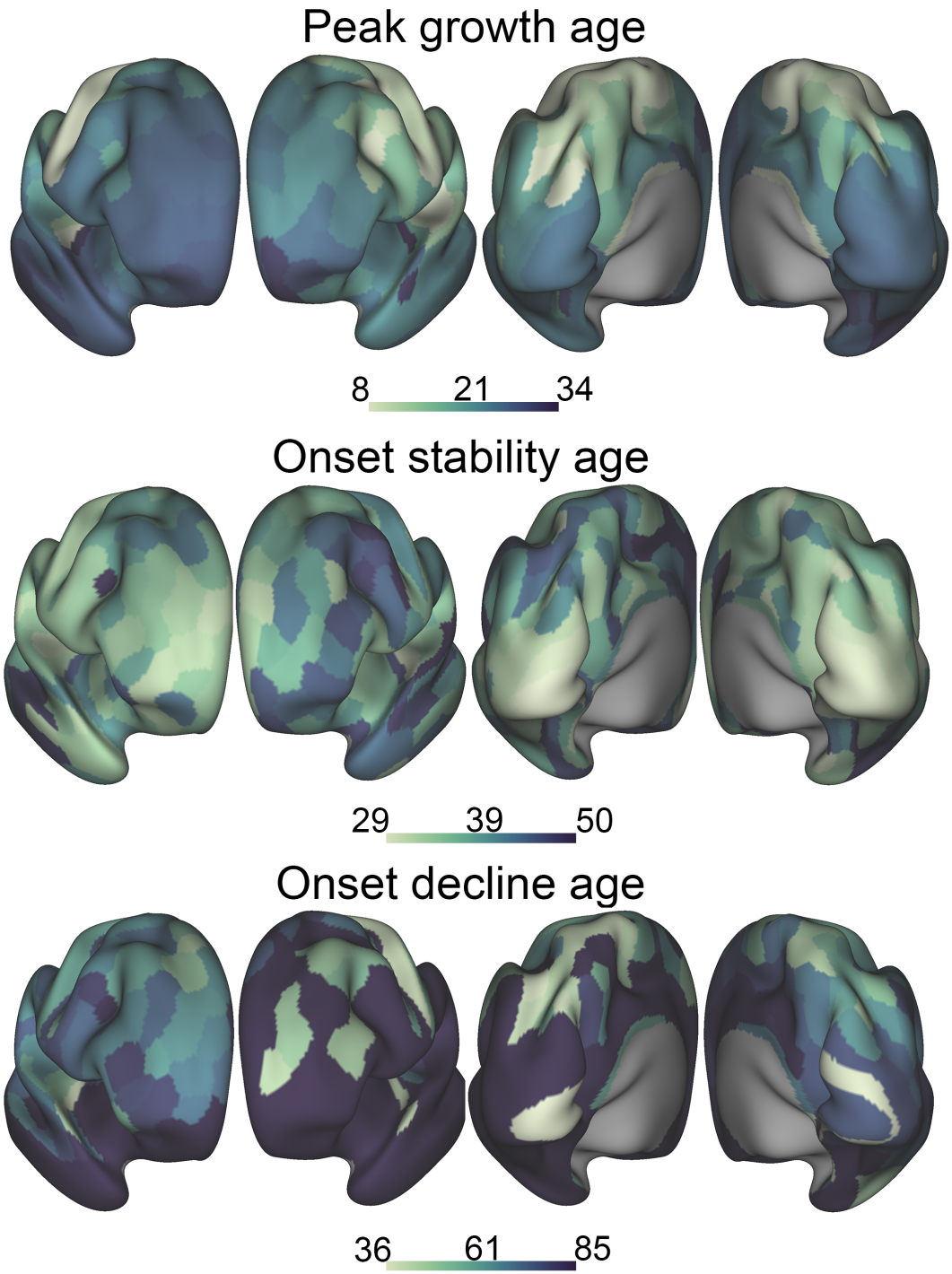

Fig. S2. Surface maps showing anterior and posterior views of peak growth age, onset stability age, and onset decline age (see also **Fig. 2A** in main text).

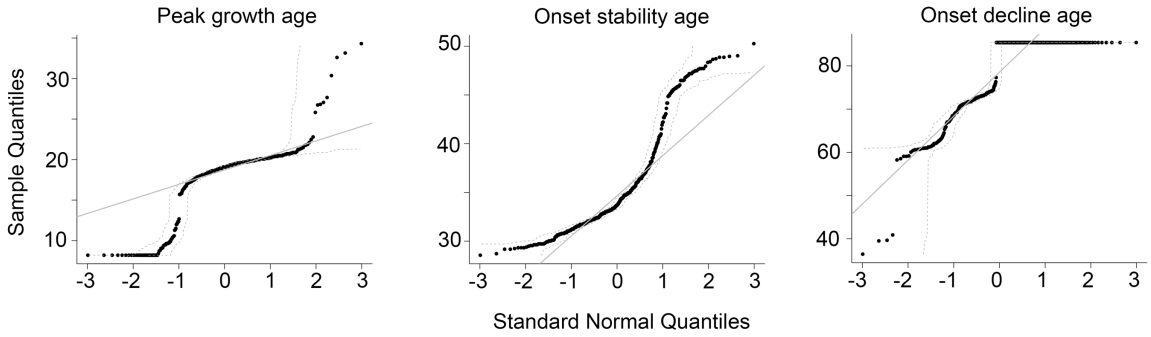

Fig. S3. Quantile-quantile plots for age at peak growth, age at onset, and decline onset. Solid grey line passes through the first and third quantile, and dotted grey lines represents 95% simultaneous confidence bands (obtained using the R package *extRemes*).

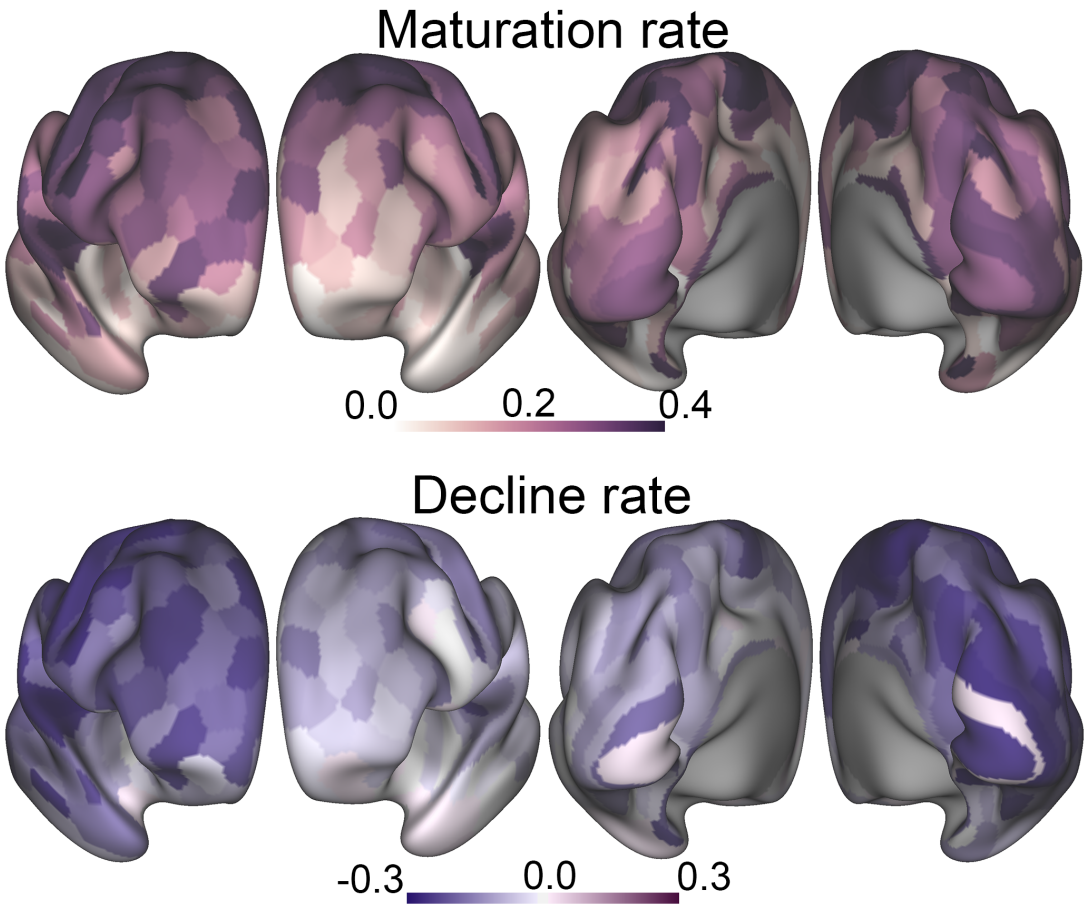

Fig. S4. Surface maps showing anterior and posterior views of rates of peak growth and decline (see also **Fig. 3A** in main text).

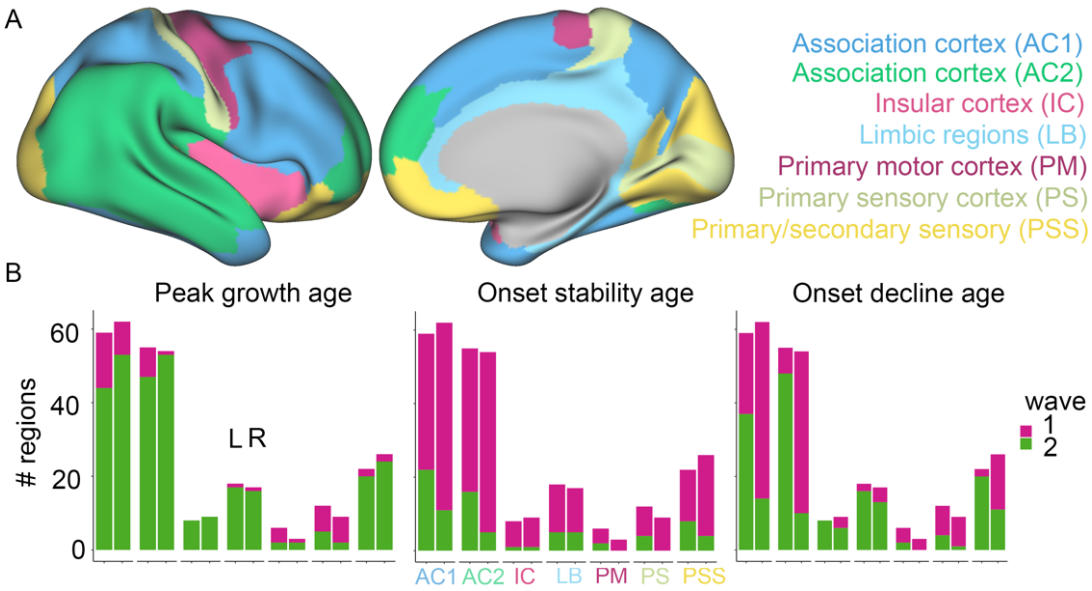

Fig. S5. A. Surface maps showing the 180 right hemisphere regions clustered in 7 cytoarchitectonic classes: AC1/2=association cortex 1/2, IC=insular cortex, LB=limbic cortex, PM=primary motor cortex, PS=primary sensory cortex, PSS=primary/secondary sensory cortex. **B**. Bar charts, for each class and hemisphere, showing number of regions in the early and late waves for peak growth age, onset stability age, and onset decline age. L/R = left/right hemisphere.

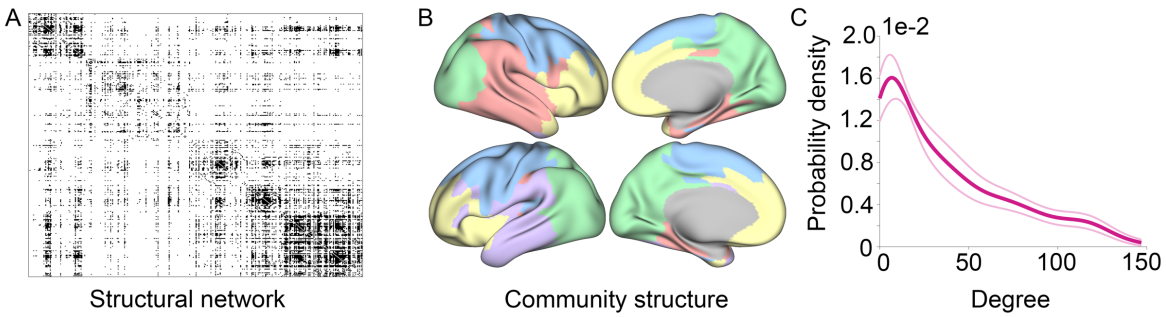

Fig. S6. **A**. A 360×360 structural covariance matrix based on correlations between all regions for the 103 participants aged between the point of maturity and decline, respectively, i.e. from 37 and 69 years. The matrix has been binarized, retaining 10% of the strongest connections or edges, shown in black, and sorted based on the community structure shown in **B**. **B**. Community structure, showing 5 distinct communities, or modules, represented in different colours. **C**. Probability density plot of the degree distribution. In this binary network, the degree is the number of connections (edges) per brain region (node). The 95% confidence bands (light

magenta) were generated by bootstrap with replacements across participants over 1000 iterations.

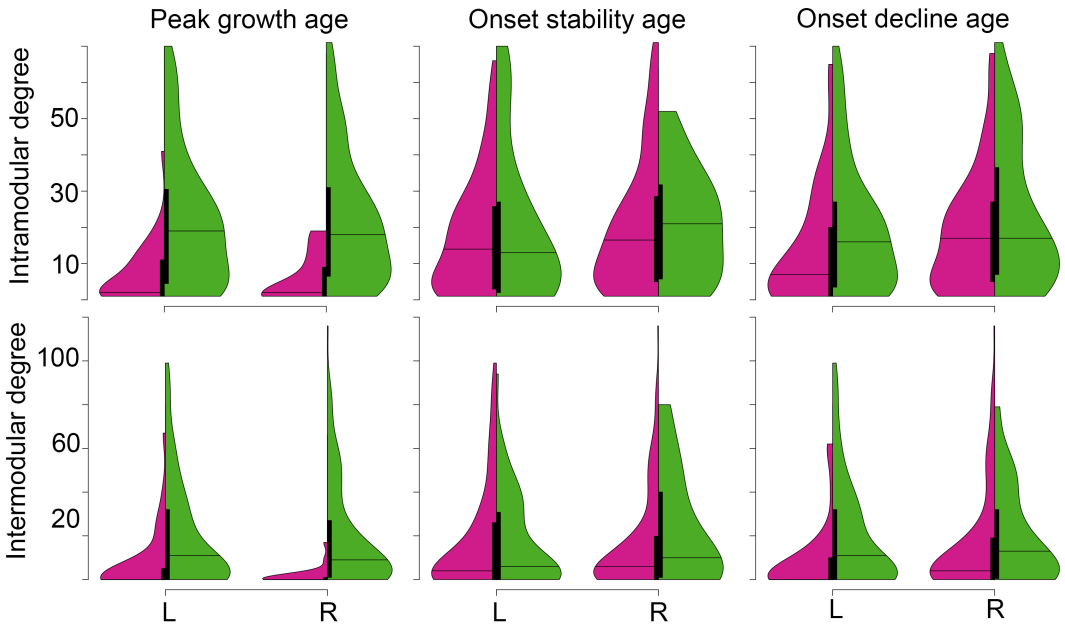

Fig. S7. Violin plots, split per hemisphere and early (magenta) and late (dark green) wave, for peak growth age, onset stability age, and onset decline age, showing distribution of intramodular degree, and intermodular degree. L, left hemisphere, R, right hemisphere. Peak growth and onset of decline occurred later in particularly global hubs (see also **Fig. 4** in main text).

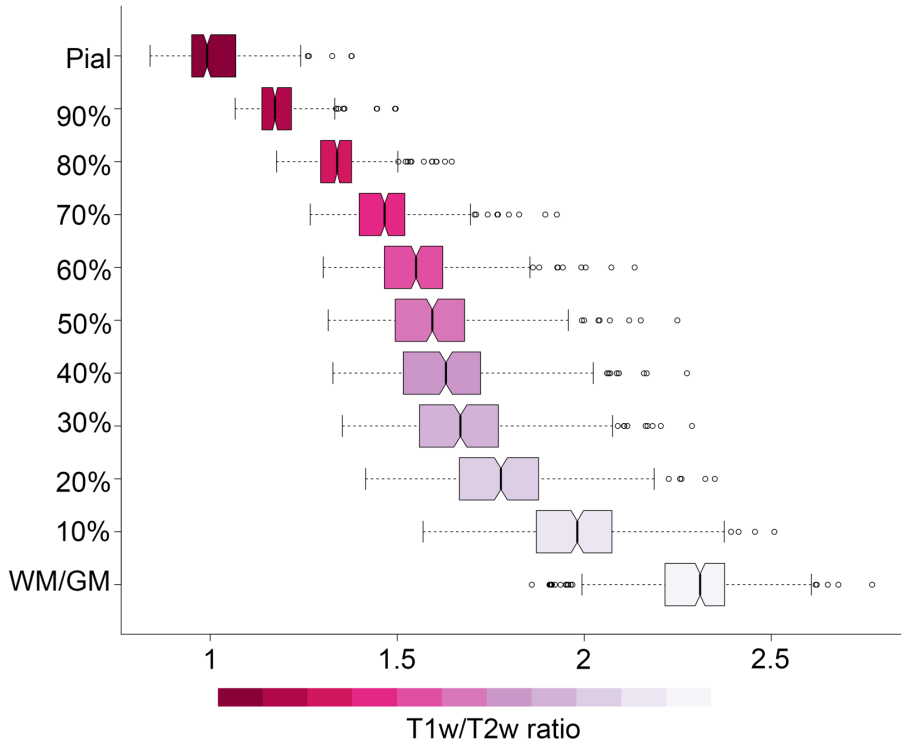

Fig. S8. T1w/T2w ratio values as a function of cortical depth.

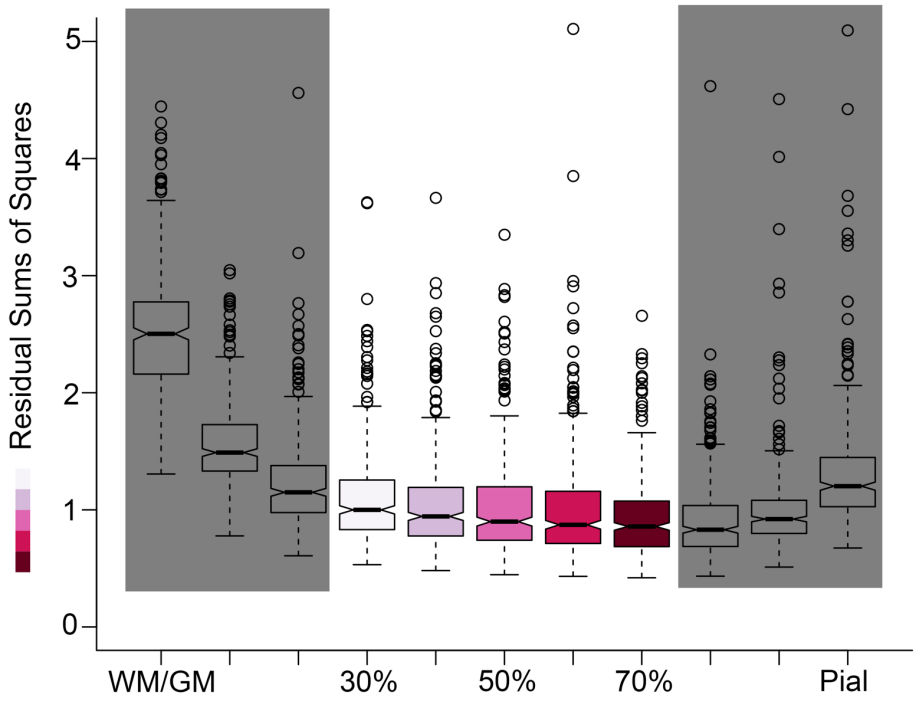

Fig. S9. Residuals (sum of squares) from spline fitting of each of the 360 cortical regions, plotted as a function of age, at each cortical depth, across the whole sample. We only considered depths between 30% and 70% (in colour) to minimize influence

of partial voluming effects from the white matter and cerebrospinal fluid, respectively (please see text for references).

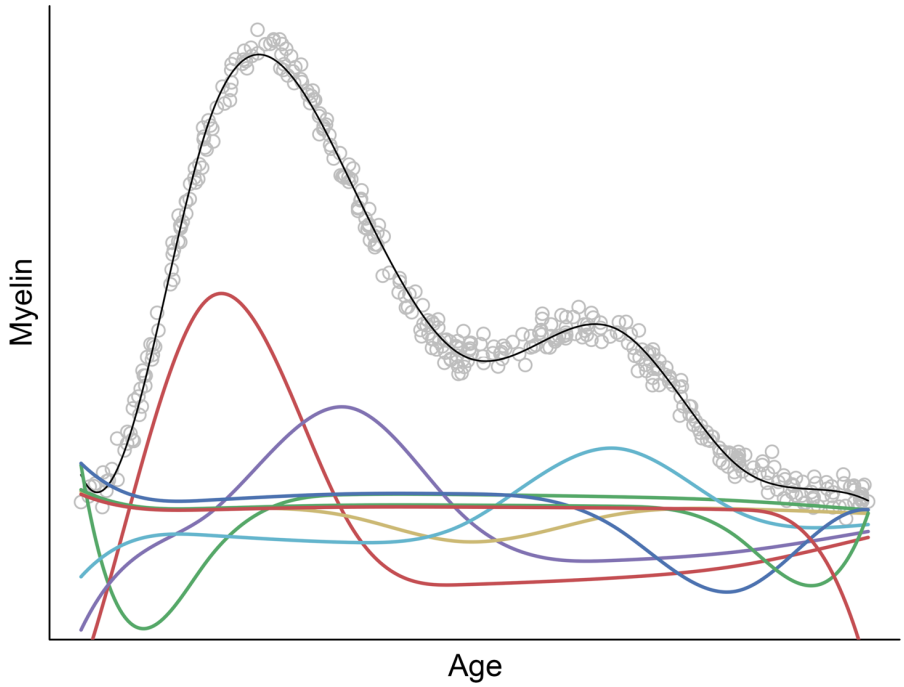

Fig. S10. Simulated data (grey circles) of a hypothetical age-myelin relationship with a fitted cubic B-spline (black curve), which is a weighted sum of the 8 basis functions, multiplied by their respective coefficients, plotted below (coloured curves).

Supplementary References

1. Tamnes CK*, et al.* (2010) Brain maturation in adolescence and young adulthood: regional age-related changes in cortical thickness and white matter volume and microstructure. *Cereb Cortex* 20(3):534-548.
2. Westlye LT, Walhovd KB, Bjornerud A, Due-Tonnessen P, & Fjell AM (2009) Error-related negativity is mediated by fractional anisotropy in the posterior cingulate gyrus--a study combining diffusion tensor imaging and electrophysiology in healthy adults. *Cereb Cortex* 19(2):293-304.
3. Tamnes CK*, et al.* (2013) Brain development and aging: overlapping and unique patterns of change. *Neuroimage* 68:63-74.
4. Beck AT & Steer R (1987) *Beck Depression Inventory Scoring Manual* (The Psychological Corporation, New York).
5. Folstein MF, Folstein SE, & McHugh PR (1975) "Mini-mental state". A practical method for grading the cognitive state of patients for the clinician. *J Psychiatr Res* 12(3):189-198.
6. Grydeland H, Walhovd KB, Tamnes CK, Westlye LT, & Fjell AM (2013) Intracortical myelin links with performance variability across the human lifespan: results from T1- and T2-weighted MRI myelin mapping and diffusion tensor imaging. *J Neurosci* 33(47):18618-18630.
7. Wechsler D (1999) *Wechsler Abbreviated Scale of Intelligence* (The Psychological Corporation, San Antonio, TX).
8. Glasser MF*, et al.* (2013) The minimal preprocessing pipelines for the Human Connectome Project. *Neuroimage* 80:105-124.
9. van der Kouwe AJW, Benner T, Salat DH, & Fischl B (2008) Brain morphometry with multiecho MPRAGE. *Neuroimage* 40(2):559-569.
10. Dale AM, Fischl B, & Sereno MI (1999) Cortical surface-based analysis. I. Segmentation and surface reconstruction. *Neuroimage* 9(2):179-194.
11. Segonne F*, et al.* (2004) A hybrid approach to the skull stripping problem in MRI. *Neuroimage* 22(3):1060-1075.
12. Fischl B & Dale AM (2000) Measuring the thickness of the human cerebral cortex from magnetic resonance images. *Proc Natl Acad Sci U S A* 97(20):11050-11055.
13. Fischl B*, et al.* (2002) Whole brain segmentation: automated labeling of neuroanatomical structures in the human brain. *Neuron* 33(3):341-355.

14. Fischl B*, et al.* (2004) Sequence-independent segmentation of magnetic resonance images. *Neuroimage* 23 Suppl 1:S69-84.
15. Fischl B, Sereno MI, & Dale AM (1999) Cortical surface-based analysis. II: Inflation, flattening, and a surface-based coordinate system. *Neuroimage* 9(2):195-207.
16. Fischl B*, et al.* (2004) Automatically parcellating the human cerebral cortex. *Cereb Cortex* 14(1):11-22.
17. Greve DN & Fischl B (2009) Accurate and robust brain image alignment using boundary-based registration. *Neuroimage* 48(1):63-72.
18. Glasser MF & Van Essen DC (2011) Mapping human cortical areas in vivo based on myelin content as revealed by T1- and T2-weighted MRI. *J Neurosci* 31(32):11597-11616.
19. Glasser MF*, et al.* (2016) A multi-modal parcellation of human cerebral cortex. *Nature* 536(7615):171-178.
20. Fischl B, Sereno MI, Tootell RB, & Dale AM (1999) High-resolution intersubject averaging and a coordinate system for the cortical surface. *Hum Brain Mapp* 8(4):272-284.
21. Robinson EC*, et al.* (2014) MSM: a new flexible framework for Multimodal Surface Matching. *Neuroimage* 100:414-426.
22. Polimeni JR, Fischl B, Greve DN, & Wald LL (2010) Laminar analysis of 7T BOLD using an imposed spatial activation pattern in human V1. *Neuroimage* 52(4):1334-1346.
23. Huntenburg JM*, et al.* (2017) A Systematic Relationship Between Functional Connectivity and Intracortical Myelin in the Human Cerebral Cortex. *Cereb Cortex* 27(2):981-997.
24. Solari SV & Stoner R (2011) Cognitive consilience: primate non-primary neuroanatomical circuits underlying cognition. *Front Neuroanat* 5:65.
25. Kritzer MF & Goldman-Rakic PS (1995) Intrinsic circuit organization of the major layers and sublayers of the dorsolateral prefrontal cortex in the rhesus monkey. *J Comp Neurol* 359(1):131-143.
26. Levitt JB, Lewis DA, Yoshioka T, & Lund JS (1993) Topography of pyramidal neuron intrinsic connections in macaque monkey prefrontal cortex (areas 9 and 46). *J Comp Neurol* 338(3):360-376.

27. Wood SN (2006) *Generalized Additive Models: An Introduction with R* (CRC Press, Boca Raton, FL).
28. Fjell AM*, et al.* (2010) When does brain aging accelerate? Dangers of quadratic fits in cross-sectional studies. *Neuroimage* 50(4):1376-1383.
29. Alexander-Bloch AF*, et al.* (2014) Abnormal cortical growth in schizophrenia targets normative modules of synchronized development. *Biol Psychiatry* 76(6):438-446.
30. Wood SN (2011) Fast stable restricted maximum likelihood and marginal likelihood estimation of semiparametric generalized linear models. *J R Stat Soc B* 73:3-36.
31. Marra G & Wood SN (2012) Coverage properties of confidence intervals for generalized additive model components. *Scandinavian Journal of Statistics* 39(1):53-74.
32. Hartigan JA & Hartigan P (1985) The dip test of unimodality. *The Annals of Statistics*:70-84.
33. Xu L, Bedrick EJ, Hanson T, & Restrepo C (2014) A comparison of statistical tools for identifying modality in body mass distributions. *Journal of Data Science* 12(1):175-196.
34. Tantrum J, Murua A, & Stuetzle W (2003) Assessment and pruning of hierarchical model based clustering. *Proceedings of the ninth ACM SIGKDD international conference on Knowledge discovery and data mining*, (ACM), pp 197-205.
35. Yarkoni T, Poldrack RA, Nichols TE, Van Essen DC, & Wager TD (2011) Large-scale automated synthesis of human functional neuroimaging data. *Nat Methods* 8(8):665-670.
36. van den Heuvel MP, Scholtens LH, Feldman Barrett L, Hilgetag CC, & de Reus MA (2015) Bridging Cytoarchitectonics and Connectomics in Human Cerebral Cortex. *J Neurosci* 35(41):13943-13948.
37. Vertes PE*, et al.* (2016) Gene transcription profiles associated with inter-modular hubs and connection distance in human functional magnetic resonance imaging networks. *Philos Trans R Soc Lond B Biol Sci* 371(1705).
38. Scholtens LH, de Reus MA, de Lange SC, Schmidt R, & van den Heuvel MP (2016) An MRI Von Economo - Koskinas atlas. *Neuroimage*.

39. Triarhou LC (2007) The Economo-Koskinas atlas revisited: cytoarchitectonics and functional context. *Stereotact Funct Neurosurg* 85(5):195-203.
40. Alexander-Bloch A, Giedd JN, & Bullmore E (2013) Imaging structural co-variance between human brain regions. *Nat Rev Neurosci* 14(5):322-336.
41. Alexander-Bloch AF*, et al.* (2010) Disrupted modularity and local connectivity of brain functional networks in childhood-onset schizophrenia. *Front Syst Neurosci* 4:147.
42. Rubinov M & Sporns O (2010) Complex network measures of brain connectivity: uses and interpretations. *Neuroimage* 52(3):1059-1069.
43. Blondel VD, Guillaume JL, Lambiotte R, & Lefebvre E (2008) Fast unfolding of communities in large networks. *J Stat Mech-Theory E*.
44. Sporns O & Betzel RF (2016) Modular Brain Networks. *Annu Rev Psychol* 67:613-640.
45. Shinn M*, et al.* (2017) Versatility of nodal affiliation to communities. *Sci Rep* 7(1):4273.
46. Benjamini Y & Yekutieli D (2001) The control of the false discovery rate in multiple testing under dependency. *Ann Stat* 29(4):1165-1188.